Archive

Steam Bubble Collapse, Water Hammer and Piping Network Response

Volume I. Steam Bubble Collapse and Water Hammer in Piping Systems: Experiments and Analysis

by

R. Gruel, W. Hurwitz, P. Huber and P. Griffith

Energy Laboratory Report No. MIT-EL 80-017

June 1980

Steam Bubble Collapse, Water Hammer and Piping Network Response

Volume I. Steam Bubble Collapse and Water Hammer in Piping Systems: Experiments and Analysis

by

R. Gruel, W. Hurwitz, P. Huber and P. Griffith

Department of Mechanical Engineering
and
Energy Laboratory

Massachusetts Institute of Technology
Cambridge, Massachusetts 02139

sponsored by

Boston Edison Company
Consumers Power Company
Northeast Utilities Service Company

MIT Energy Laboratory Report No. MIT-EL 80-017

June 1980

Foreword

Work on steam bubble collapse, water hammer and piping network response was carried out in two closely related but distinct sections. Volume I of this report details the experiments and analyses carried out in conjunction with the steam bubble collapse and water hammer project. Volume II details the work which was performed in the analysis of piping network response to steam generated water hammer.

Table of Contents

Volume I

Steam Bubble Collapse and Water Hammer
in Piping Systems: Experiments and Analysis

I. Introduction

Water hammer incidents in conventional and nuclear steam systems are an important problem of broad general interest in piping network design and transient operation. Water hammer in PWR steam generator sparger feed lines has, for example, been a recurrent problem when the sparger becomes uncovered during certain operational transients (Creare 1977). The central goal of this research has been to develop experimental data and supporting analyses that will contribute to the evolving understanding of water hammer created by steam bubble entrapment in a pipe containing subcooled liquid.

The first objective of this study has been to obtain a body of experimental data on water hammer initiated by steam bubble collapse. These experiments include measurement of pressure transients and high speed films of the process of bubble collapse and impact, and, in conjunction with Hurwitz (1980), records of the resultant pressure wave propagation through a variety of simple piping configurations and measurements of the induced structural response. The data that have been obtained should be useful in benchmarking existing analytic models and numerical codes.

The second objective of this study has been to formulate and test simple models for the steam bubble collapse process. The starting point in the analysis of water hammer is obtaining a source "forcing function" which ultimately produces loads on remote as well as on nearby elements of the piping system. Back pressure (the system absolute pressure outside the condensing steam bubble) and flow resistance in the line in which the collapse occurs have been varied experimen-

tally and analyzed via a hydrodynamic model for steam bubble collapse. Simple scaling laws correlating the effects of varying back pressure and flow resistance to impact pressures and bubble collapse times have been derived from this model and compared with the experimental data.

Finally, water slug and steam bubble dynamics are combined to predict the bubble collapse dynamics as a function of heat transfer rates from the steam to the subcooled liquid. These predictions are compared with the experimental results. Two physical limits to the heat transfer rates can be postulated, predicted and compared with the heat transfer rates required to match theory and experiment. The predicted limits consistantly bound the valves inferred from experiment.

II. Experimental Apparatus

Figure 1 shows a schematic of the water hammer generator. It is constructed of standard 1-1/2" steel pipe and fittings, with a transparent lexan section (1-1/2" I.D. - 1-3/4" O.D.) in which the final phase of bubble collapse and column impact occurs. In the initial state, a short liquid column fills the lower part of the system with its free surface adjusted to lie within the lexan section. Above this is a long steam bubble, initially in thermal equilibrium with the lower liquid-free surface. A fast-acting, pneumatically operated piston valve separates the top of the steam cavity from the cold water reservoir. The actuation of this valve brings the steam into abrupt contact with the subcooled liquid. Driven by the steam condensation, water flows rapidly from the reservoir into the central structure and collides with the lower liquid column.

The central structure consists of a series of nipples, crosses and unions. Two of these unions are specifically designed to provide a rigid, watertight interface between the lexan and steel piping.

Between the lexan section and the cold water reservoir lie two crosses. Three of the resulting four ports are utilized; one for steam inlet and one for steam outlet connections; the third is a thermocouple port. A manual ball valve and an electrical solenoid valve are located in series on both the steam inlet and outlet lines to insure isolation during the transient.

Another cross lies below the lexan section, at the end of the central structure. Two of its ports are for pressure transducers;

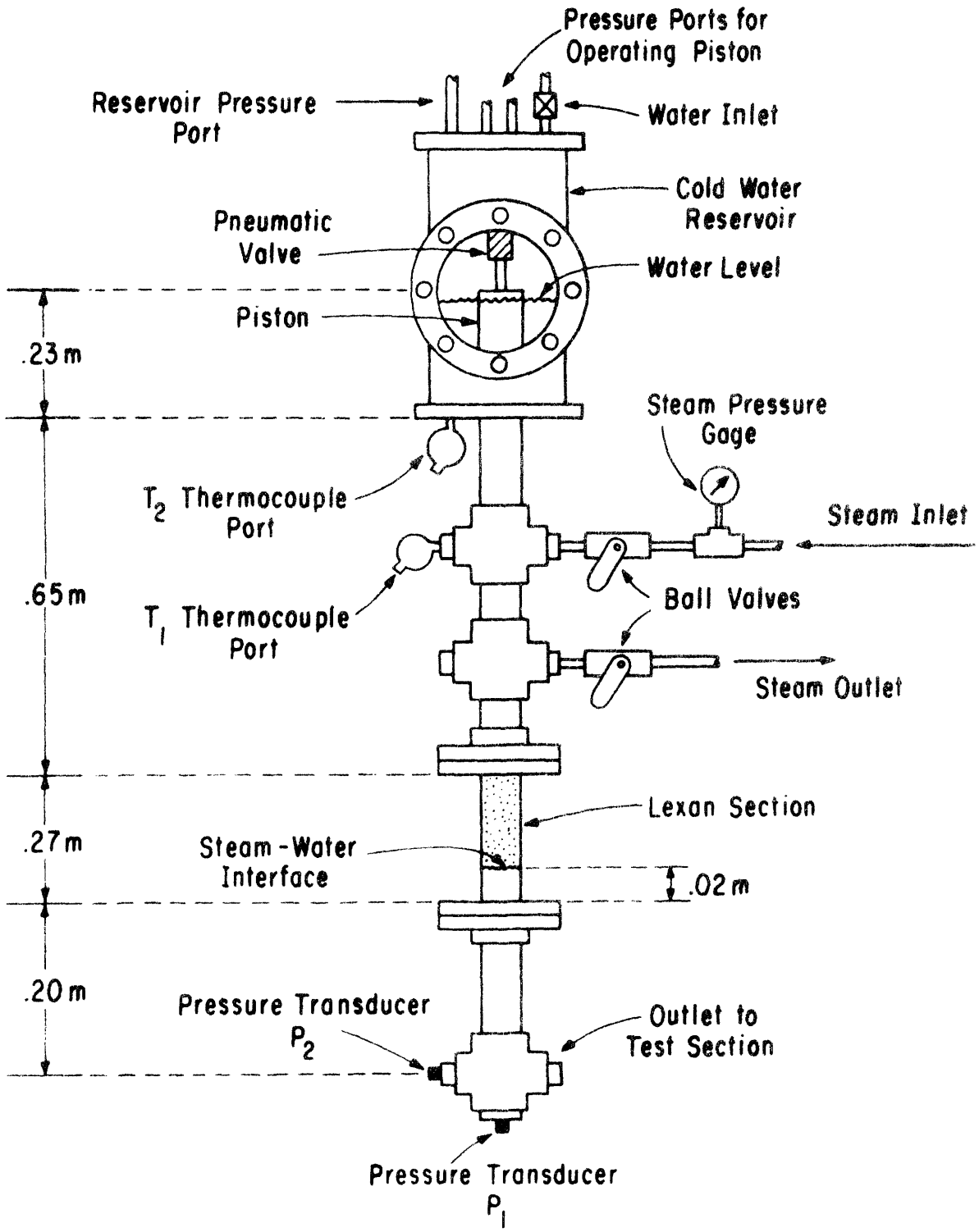

Figure 1. Schematic of Water Hammer Generator

the other is attached to the piping network whose response to the water hammer is being tested (Figure 2).

The central structure is rigidly supported by a framework constructed from 1-1/4" pipe and special interconnecting fittings. The framework is about 1' in depth and width and stands about 6' tall. Its four legs are securely bolted to the floor. In addition, four braces (one on each leg) run from the mid-section of the framework to the floor where they are also rigidly bolted down. Pipehangars and threaded rods are utilized to keep the central structure from vibrating in any horizontal direction. The cold water reservoir and the auxilliary pressure stabilization tank are also supported by this structure.

The cold water reservoir, consisting of a standard 6", 125 psi drainage tee, is mounted above the central structure. It is aligned vertically so that the side port can be used to view the water level inside the tee. Initially, water fills about half the tee; pressurized nitrogen fills the rest. An auxilliary tank is used to insure that the initial and final pressures in the system vary by less than 5%.

A pneumatic valve is mounted within the reservoir. It is a double-acting valve: pressure can be applied to push down the piston sealing it against the bottom flange (closed), or to quickly lift it off the bottom flange bringing the steam into contact with the subcooled liquid (open). Nitrogen is used to operate the valve. Two pressures are utilized; 60 psig to close the valve, 400 psig to open it. Originally, only 120 psig was used to open the valve, but when 250 psig was used there was a marked difference in the resulting

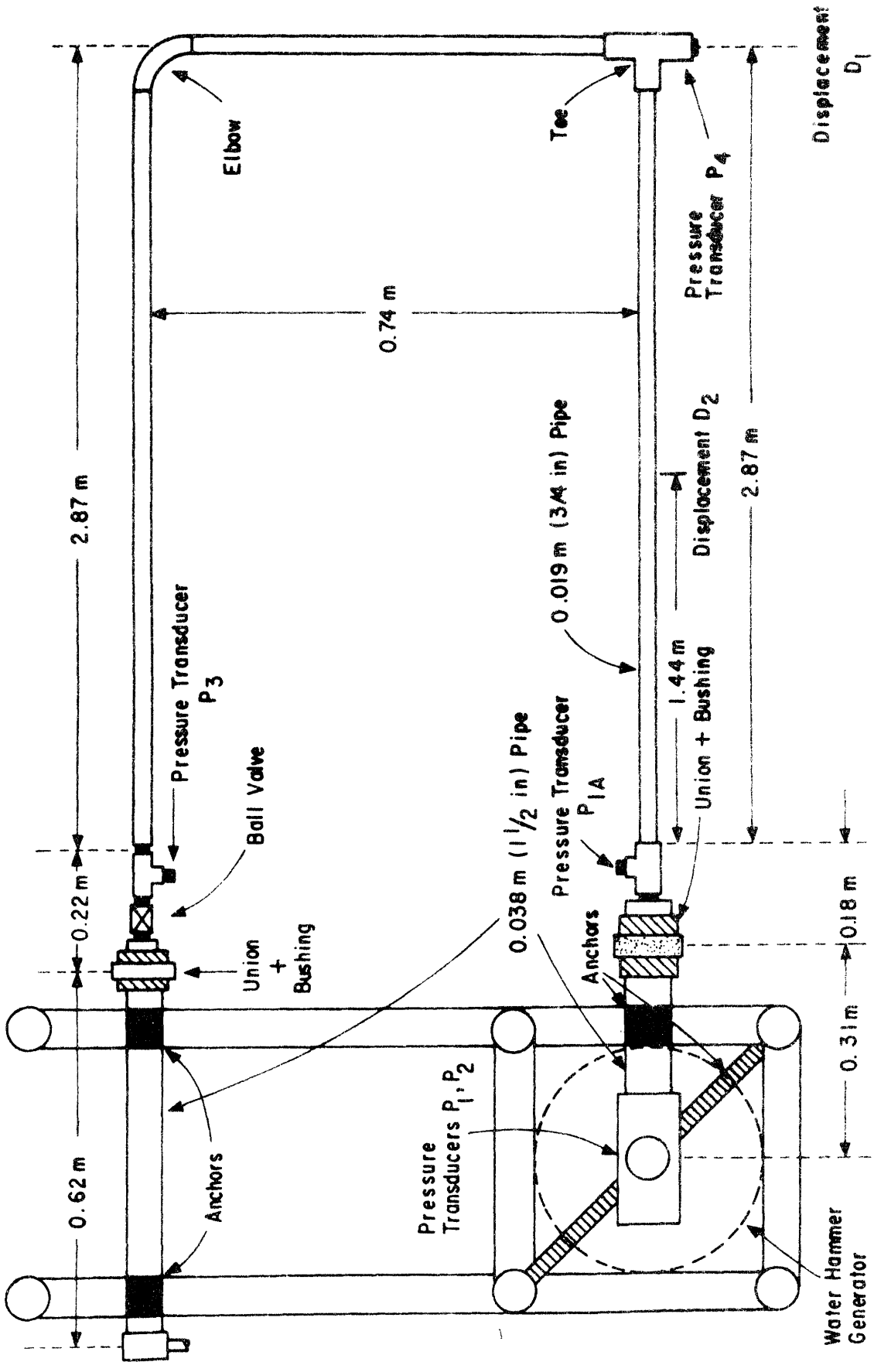

Figure 2. Piping Network Configuration

pressure histories. No further change was found when 400 psig was used, but this higher pressure was chosen to minimize any possible effect a "slow" valve might have on the pressure histories.

Attached to the pneumatic valve is an aluminum rod and disk. To minimize drag and vortex formation when the disk is lifted, a cylinder of closed-cell foam, having the same diameter of the disk, encases the rod. The top of this foam cylinder lies above the water level in the reservoir, thereby reducing the drag when the valve is opened.

The bottom of the aluminum disk is covered with soft rubber which provides a good seal when compressed against the bottom flange of the reservoir. This flange provides the interface between the 6" tee (reservoir) and 1-1/2" pipe (central structure). An orifice plate can be mounted on the upper surface of the bottom flange - the piston would then seal against this plate. To provide a good seal between the orifice plate and the bottom flange, the flange was machined to hold an O-ring between it and the plate. Thus, when the piston is closed, both the soft rubber and O-ring are compressed, insuring that the cold water in the reservoir is isolated from the saturated steam in the central structure.

III. Instrumentation

Instrumentation on the generator can be separated into two categories - initial state measurement and transient response recording. Initial state measurements were made with pressure gauges and thermocouples. The transient response was recorded using pressure transducers and high-speed films.

Two static pressure gauges having a range of 0-60 psig (100-500 kPa) were used on the generator. One was used to measure the initial pressure in the steam bubble (Figure 1). The other measured the back pressure in the cold water reservoir (P_o; this gauge was located on the auxilliary tank and is not shown in Figure 1).

Initial temperatures were also measured in the cold water reservoir (T_2, Figure 1) near the bottom flange and in the steam bubble (T_1, Figure 1) opposite the steam inlet. Iron-constantan thermocouples were used in conjunction with an artificial ice point. The signal was fed into a digital readout, displaying the voltage output of the thermocouple. No transient temperature histories were recorded.

Pressure transients were recorded using piezoelectric pressure transducers with response times (3μs) considerably shorter than any of the transients of interest. Two ranges of transducer sensitivity were used to capture details of both the steam bubble collapse transient (involving pressure changes of order 10^2 kPa (15 psi) over a period of order 10^2 ms) and the column impact (involving pressure changes of order 10^4 kPa (1500 psi) over a period of order 1 ms). Four pressure transducers were used; one to measure the collapse

transient (P_2, Figure 1) and the other three to measure the column impact (P_1, Figure 1) and the wave propagation through the piping network (P_{1A}, P_3; Figure 2). These transducers were coupled (one or two at a time) to a two-channel storage oscilloscope.

High-speed films (1000-2000 frames per second) of the final phase of bubble collapse, column impact, and subsequent cavitation and column separation were obtained and correlated with measured pressure transients.

IV. Operating Procedure

Initial conditions in the test system were accurately set and recorded before a water hammer was generated. The following operating procedure was used.

The desired reservoir conditions were set first. Both the piston valve and the drain valve were opened and water was injected into the reservoir. This flushed the air out of the piping network and brought cold water into the reservoir. When the water in the reservoir was sufficiently cold (20-25°C), the drain valve and piston valve were closed. The water supply was shut off when the water level in the reservoir reached the desired height. Nitrogen was then injected into the pressure equilization tank until the desired pressure was reached (300-500 kPa).

A steam pocket was formed by opening both the steam inlet and steam outlet valves. The incondensible gas and steam in the supply line along with the water above the steam outlet port in the central structure were carried through the outlet line to the steam dump tank. This was continued for several minutes until only steam flowed through the line. The steam supply was from the M.I.T. steam lines at a pressure of 1500 kPa and temperature of 200°C. The air fraction in this steam is typically about 10^{-4}. The steam outlet valve was closed and the drain was opened slightly to lower the water level so that the water/steam interface was within the lexan section. The steam pressure was set by adjusting a regulator on the steam supply line. The water/steam interface was allowed to reach a local thermal equilibrium.

The temperature and pressure in the steam were then checked to ascertain that it had reached saturation conditions, and the reservoir temperature and pressure were recorded. T_2 ranged from 20-25°C and P_o was set at various 50 kPa increments between 300 kPa and 500 kPa. The manual ball valve on the steam inlet line was closed, and immediately afterward the solenoid valve on the same line was closed simultaneous to the opening of the piston valve. This allowed the steam bubble collapse and subsequent column impact to occur in a controlled, repeatable manner.

V. Results

The oscillogram in Figure 3 shows a typical pressure transient developed during bubble collapse and column impact. Pressure transducer P_2 shows the details of the bubble collapse pressure drop (upper trace) in the time interval -220 ms > t > 0. Pressure transducer P_1 records the impact pressures (lower trace), the first of which begins at $t \equiv 0$. Note the different scales for the two traces.

Figure 4 shows a sequence of line drawings traced from a high-speed film record of bubble collapse and column impact under conditions similar to those depicted by the oscillogram. In view of the generally excellent test-to-test repeatability that has been achieved, the film records should correlate reasonably well with the details of the pressure histories, although they were obtained in separate runs. All times are referenced to the impact time $t \equiv 0$; valve opening can also be inferred in the high-speed films from the almost immediate onset of boiling at the surface of the lower liquid column caused by the rapid depressurization of the steam cavity. Valve opening is also characterized by the initial rapid pressure drop in the steam cavity (P_2, $t < -220$ ms). The high degree of subcooling in the reservoir and the large interface area and turbulent mixing produced when the valve is opened accounts for this rapid initial depressurization.

The subsequent pressure drop rate decreases rapidly ($t < -220$ ms) due to two separate effects. When the subcooled liquid/steam interface enters the central structure, a thermal boundary layer develops at the interface, slowing the rate of condensation. Boiling at the lower interface also reduces the effective overall rate of mass

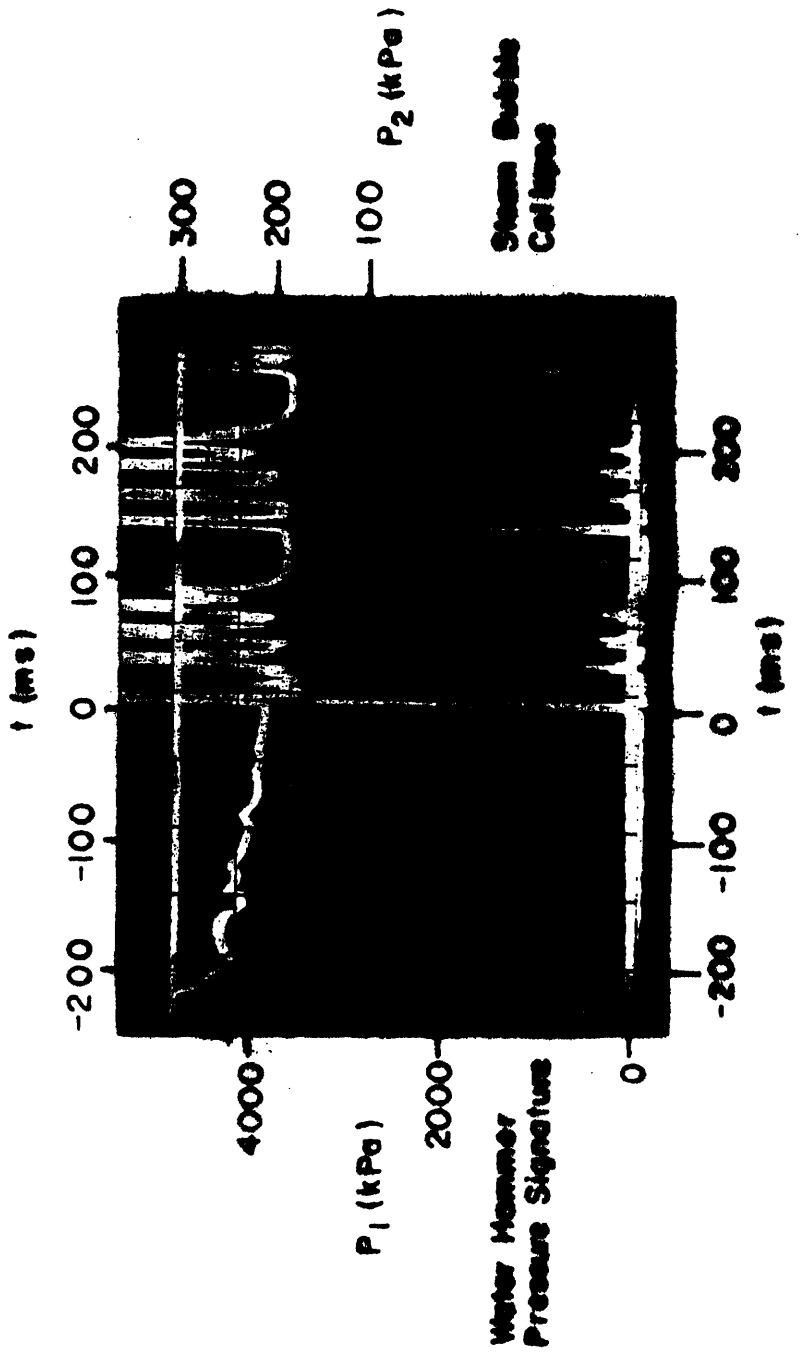

Figure 3. Typical Water Hammer Pressure Signature

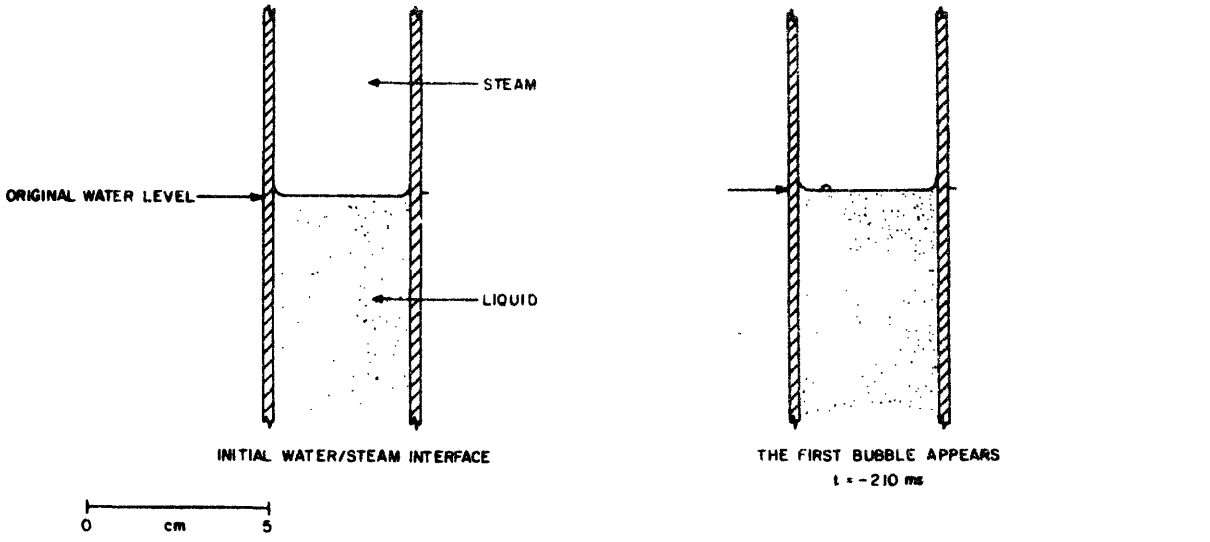

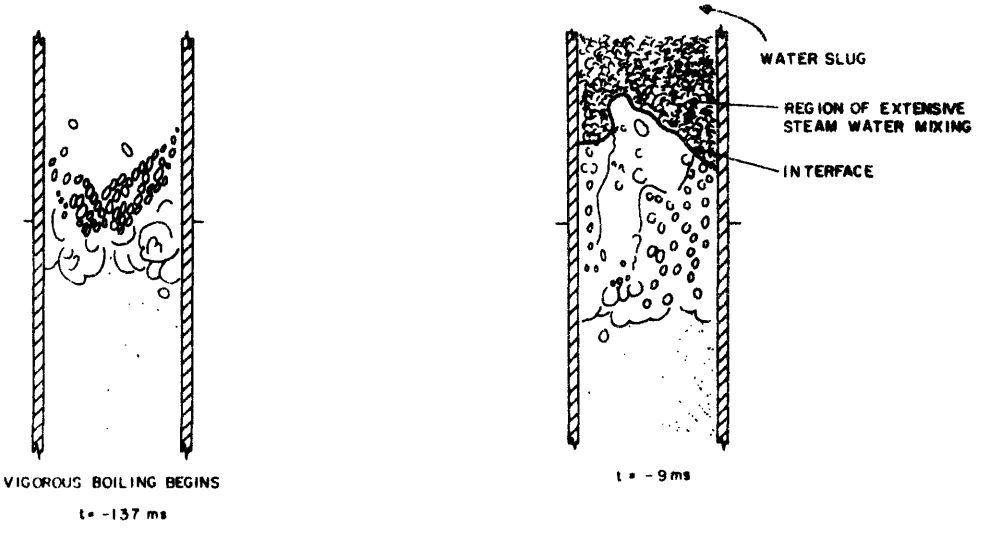

Figure 4. Sequence of Events through the Formation of the First Cavitation Bubbles traced from a High Speed film taken at 1000 frames per second.

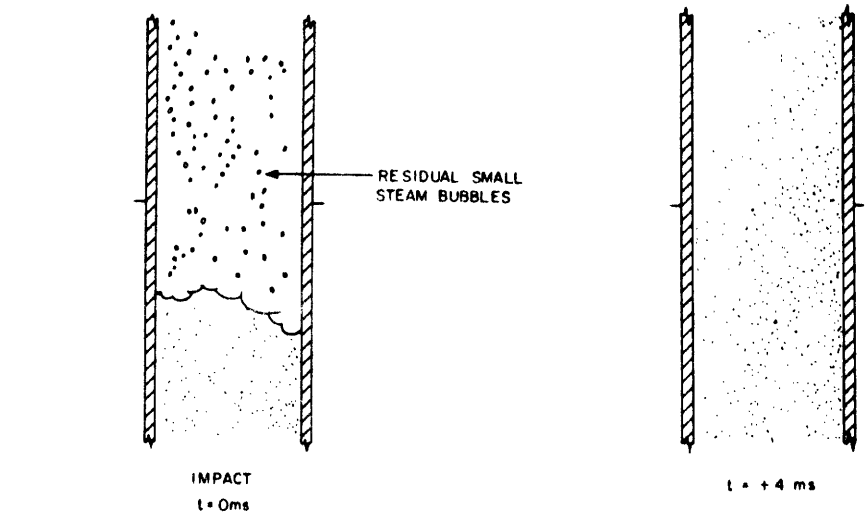

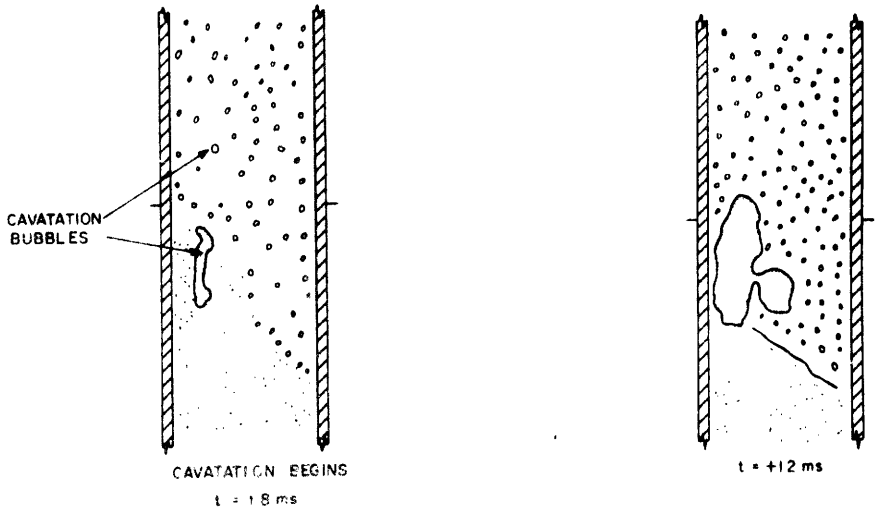

Figure 4. continued

removal from the steam cavity. The high-speed films (Figure 4) show that a significant amount of water is boiled off the lower surface at this time - the interface drops 2-3 cm during bubble collapse. The total collapse time inferred from either the pressure history P_2 or the film records was approximately 220 ms for this case.

The impact time ($t \equiv 0$ in Figures 3 and 4) is self-evident in the pressure histories and can be clearly identified in the high-speed films. Impact pressures are of typical acoustic levels - approximately 4000 kPa in this case (P_1, Figure 3).

Cavitation begins shortly after impact ($t \approx 8$ ms, Figure 4). Column separation ($\approx$ 130 ms long in this case) occurs very close to the point of initial impact as can be seen from the line drawings (Figure 4) and ends in column collapse producing a second impact pressure typically of lower amplitude than the initial impact pressure. This cavitation/collapse cycle is recurrent; the time between pressure spikes generally remains constant while the impact pressures decay in amplitude. This process can be seen by examining Figure 3; pressure spikes can be seen at 130 and 260 ms in the bottom trace - the related cavitations can be seen in the upper trace.

A series of experiments was conducted to investigate the effects of changes in the reservoir pressure or increases in the flow resistance between the reservoir and the central structure on the transient responses. Figures 5 and 6 illustrate some of the results. For the tests shown in Figure 5, the reservoir pressure was varied from 300 kPa to 500 kPa while the flow resistance was held constant. For the tests shown in Figure 6, the reservoir pressure was constant at 500 kPa while flow resistance was varied by inserting orifice plates in the reservoir,

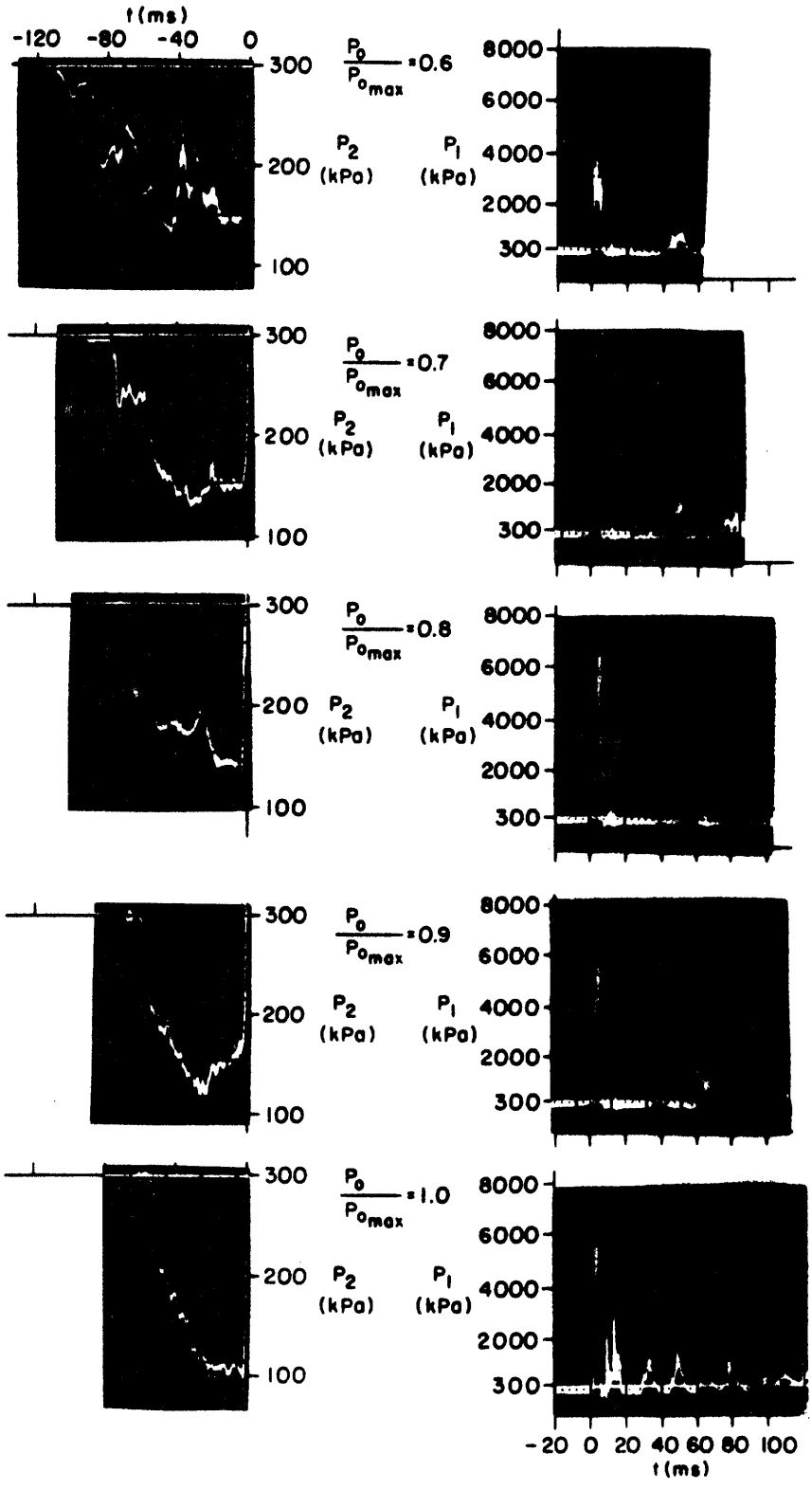

Figure 5. Water Hammer Pressure Signatures (P_1, P_2) for $T_1 \simeq 133°C$, $T_2 \simeq 20°C$, and various back pressures (P_o) where $P_o max \equiv 500$ kPa.

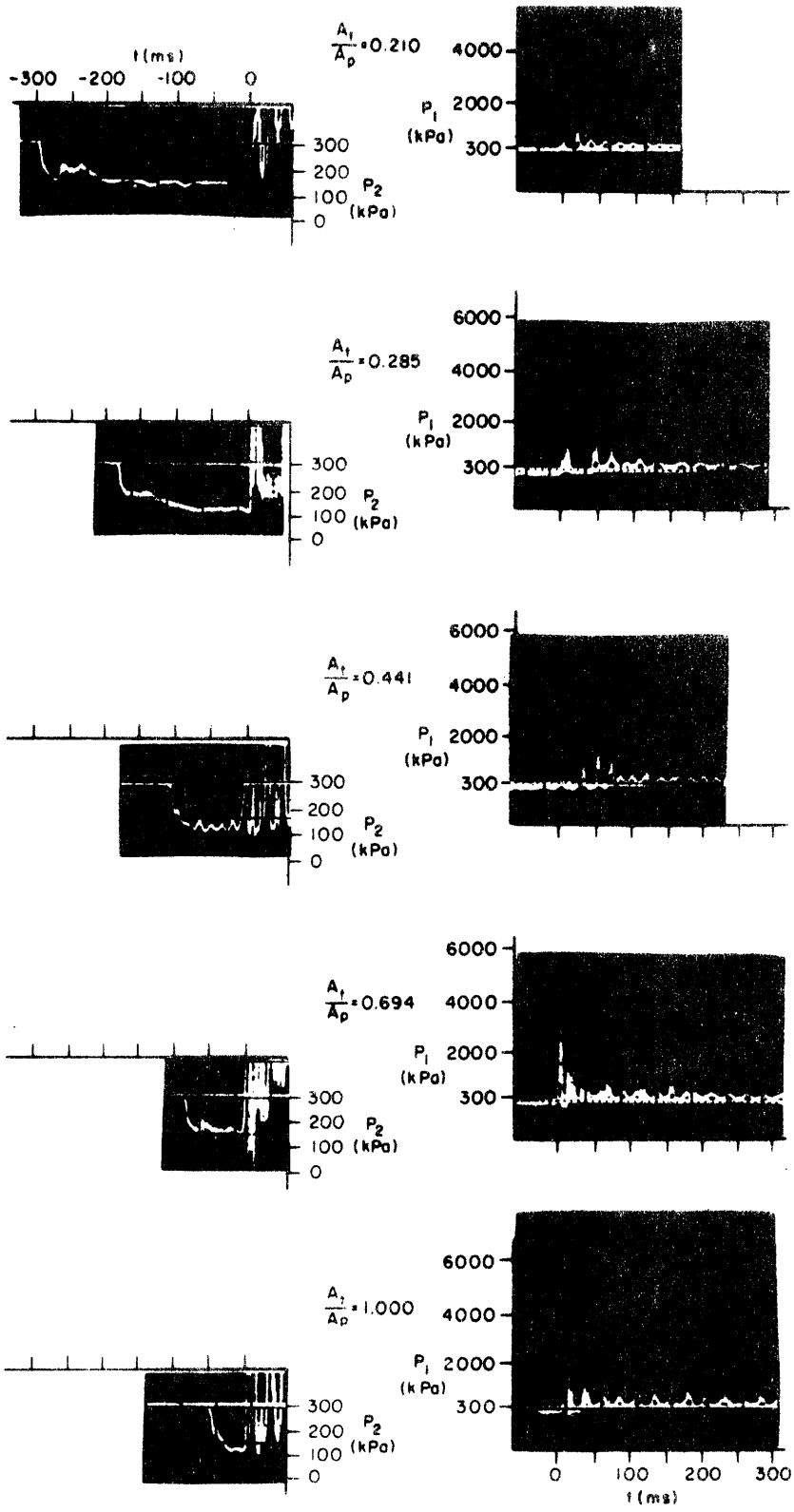

Figure 6. Water Hammer Pressure Signatures (P_1, P_0) for $T_1 \simeq 133°C$, $T_2 \simeq 20°C$, $P_0 \simeq 300$ kPa, and various flow resistances (A_t) where $A_p \equiv 11.4$ cm^2.

directly above the bottom flange. Higher back pressures and lower flow resistances clearly result in shorter collapse times and larger impact pressures.

The trends exhibited by these results can be related to a simple hydrodynamic model for the steam bubble collapse and column impact. The mass flowrate through an orifice can be expressed as

$$\dot{m} = KA_t\sqrt{2\rho_\ell \Delta P} \tag{1}$$

where K is the discharge coefficient, A_t is the area of the orifice, ρ_ℓ is the density of the liquid, and ΔP is the pressure drop ($P_o - P_2$) across the orifice plate (Baumeister and Marks Seventh Edition). K is assumed constant for the various orifice plates as a first approximation and the exact value of ΔP will depend on the heat transfer dynamics in the central structure but will scale with P_o.

The collapse time t_c is inversely proportional to the volume flowrate; Equation (1) therefore suggests

$$t_c \propto \frac{1}{A_t \sqrt{P_o}} \tag{2}$$

The impact pressure P_I is proportional to the column velocity at impact and should therefore scale roughly as the inverse of the collapse time:

$$P_I \propto A_t \sqrt{P_o} \tag{3}$$

The maximum value of $A_t\sqrt{P_o}$ in these experiments corresponded to the test in which no orifice was used ($A_t = A_p$) and the reservoir pressure was at its maximum value ($P_o max$ = 500 kPa). Normalized variables can be derived by taking the ratio of $A_t\sqrt{P_o}$ to $A_p\sqrt{P_o max}$ for the various cases. These variables correspond to the ratios of peak impact pressures ($P_I/P_I max$) and inversely to the ratios of the collapse times ($t_c min/t_c$), where $P_I max$ and $t_c min$ were the largest peak impact pressure and the shortest collapse time attainable, respectively. The experimental data normalized in this way are tabulated in Table 1 and plotted in Figures 7 and 8. The scaling laws motivated in this very simple way appear to be quite satisfactory, as judged from the rough linearity of Figures 7 and 8.

The assumption that K is constant is, of course, true for the cases in which no orifice plate was used ($K = K_p$), but it becomes increasingly inaccurate as sucessively smaller orifice plates are used ($K_p \simeq 0.82$ if no orifice is used and decreases to $K_t \simeq 0.68$ for the smallest orifice). This correction to the data is shown in Table 1, and has the effect of shifting the appropriate data points to the left on Figures 7 and 8. This shift would have little effect on these figures, although the linearity of Figure 7 is actually improved.

Table 1: Summary of collapse time and peak impact ratio calculations.

$A_t(cm^2)$	$P_o(kPa)$	$\frac{A_t\sqrt{P_o}}{A_p\sqrt{P_o min}}$	$\frac{K_t A_t\sqrt{P_o}}{K_p A_p\sqrt{P_o max}}$	$t_c(ms)$	$\frac{t_c min}{t_c}$	$P_I(kPa)$	$\frac{P_I}{P_I max}$
2.39	500	.210	.174	290	.193	1000	.137
3.25	500	.285	.250	185	.303	1700	.233
5.03	500	.441	.425	115	.487	3400	.466
6.31	500	.553	.540	100	.560	3800	.521
7.92	500	.694	.686	80	.700	4200	.575
11.40	500	1.000	1.000	56	1.000	7300	1.000
11.40	450	.949	.949	60	.933	7050	.966
11.40	400	.895	.895	62	.903	7000	.959
11.40	350	.836	.836	74	.757	6300	.863
11.40	300	.774	.774	92	.609	4000	.548

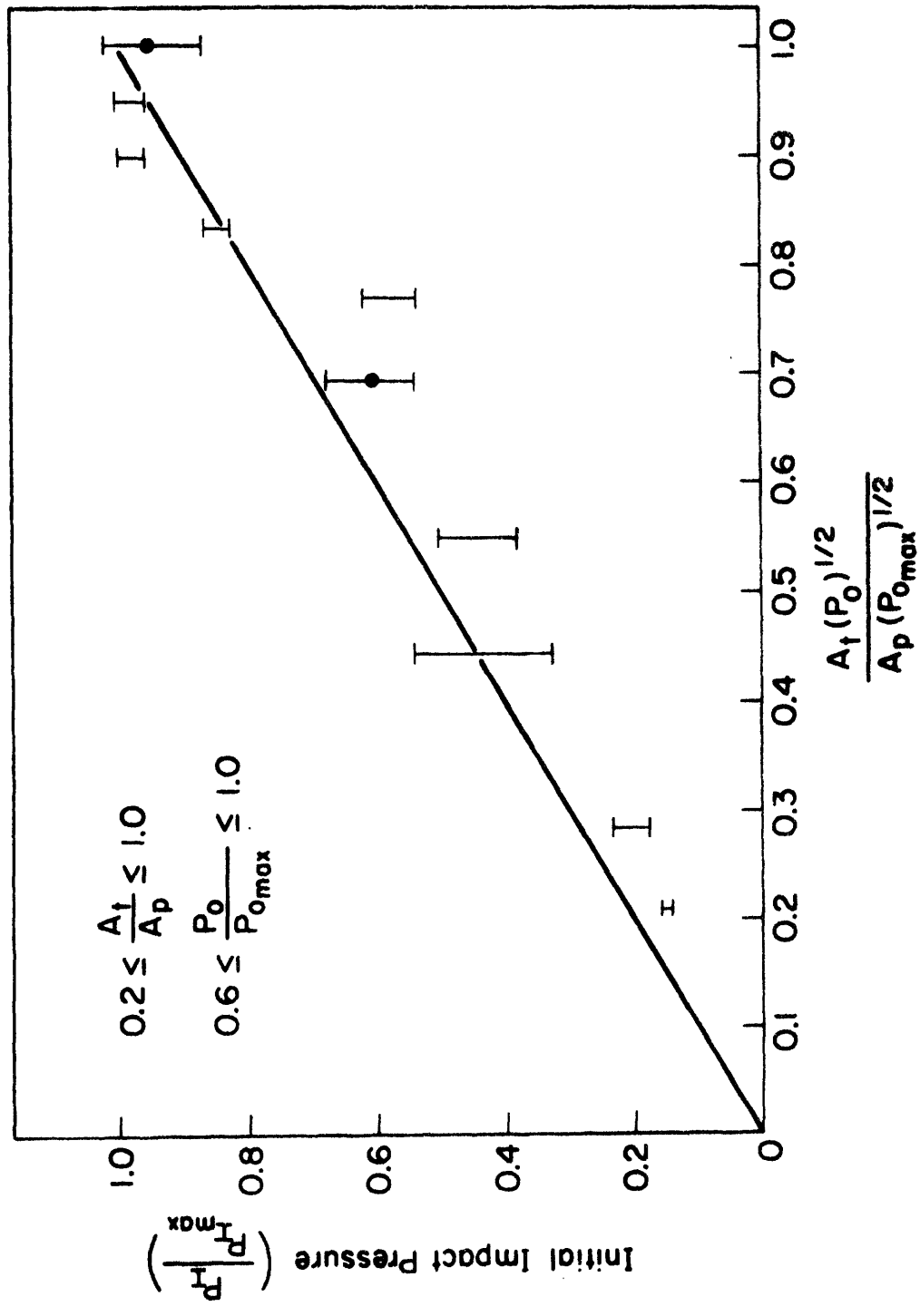

Figure 7. Effect of Varying Back Pressure and Flow Resistance on Initial Impact Pressure

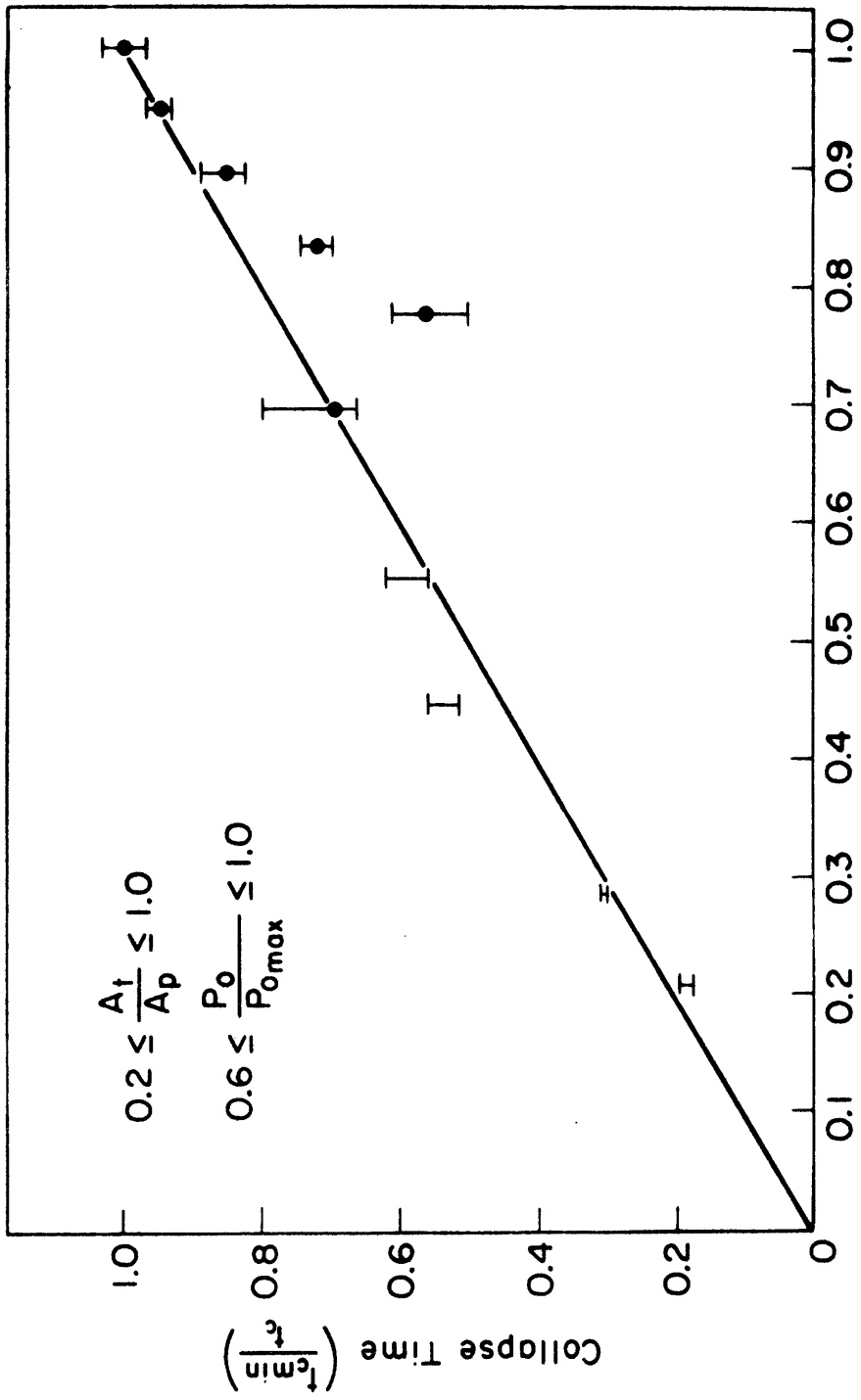

Figure 8. Effect of Varying Back Pressure and Flow Resistance on Bubble Collapse Time

VI. Modeling

The steam bubble collapse process, quite complex in reality, can be modeled by applying idealized governing equations for the momentum in the water slug and the continuity, state and energy of the steam bubble (Figure 9). The resulting four differential equations can be solved numerically.

The dynamics of the water slug are determined by the unsteady Bernoulli equation

$$P_o/\rho_\ell + gh = P_s/\rho_\ell + 1/2\ (1+k)V^2 + x\frac{dV}{dt} \qquad (4)$$

where P_o is the reservoir pressure, ρ_ℓ is the density of the liquid, g is the acceleration due to gravity, h is the height of water in the reservoir, P_s is the pressure in the gas bubble, k is a localized loss coefficient, V is the fluid velocity in the central structure, and x is the distance the fluid has traveled in the central structure (Figure 9). In this system the only viscous loss accounted for is at the entrance to the central structure (x = 0).

Continuity for the steam bubble requires that the mass flux out of the steam bubble equal the rate of change of mass in the bubble:

$$-\dot{m}_c = \frac{d}{dt}(\rho_s A(\ell_o - x)) \qquad (5)$$

where $\dot{m}_c$ is the net steam mass condensation rate, ρ_s is the density of the steam, A is the cross-sectional area of the central structure, and ℓ_o is the initial length of the steam bubble (Figure 9).

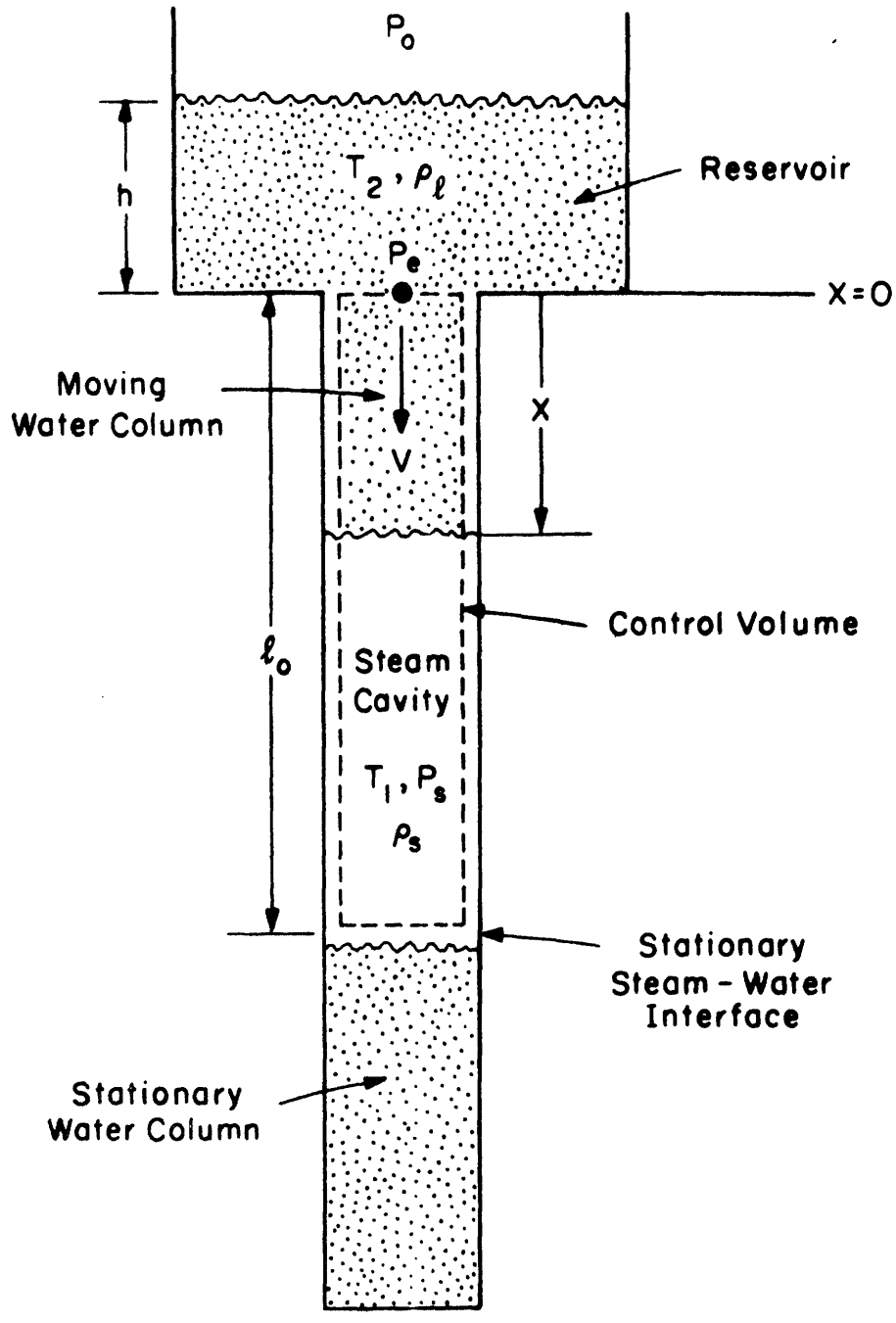

Figure 9. Control Volume for Collapse Dynamics

The state equation for the steam can be greatly simplified if the steam is modeled as an ideal gas:

$$P_s = \rho_s R T_1 \tag{6}$$

Here R is the gas constant and T_1 is the temperature of the steam, assumed uniform throughout the bubble (Figure 9).

The energy equation for the steam bubble is written as

$$\frac{d}{dt}(\rho_s A(\ell_o - x)c_v T_1) = -\dot{m}_c c_p T_1 - P_s \frac{d}{dt}(A(\ell_o - x)) \tag{7}$$

where c_p and c_v are the specific heats of the gas under constant pressure and volume, respectively.

Equations (4) - (7) can be nondimensionalized in terms of the following variables:

$$P^* = P_s/P_o \qquad \rho^* = \rho_s/\rho_s(0)$$
$$T^* = \rho_s(0)RT_1/P_o \qquad V_a = (P_o/\rho_\ell)^{1/2}$$
$$x^* = x/\ell_o \qquad t^* = V_a t/\ell_o$$
$$V^* = V/V_a = \frac{dx^*}{dt^*} \qquad c^* = \dot{m}_c/\rho_s(0)AV_a$$

The dimensionless governing equations (see Appendix I for derivation) are thus:

$$1 = P^* + 1/2\ (1+k)\left(\frac{dx^*}{dt^*}\right)^2 + x\frac{d^2x^*}{dt^{*2}} \tag{8}$$

$$-c^* = \frac{d}{dt^*}(\rho^*(1-x^*)) \tag{9}$$

$$P^* = \rho^* T^* \tag{10}$$

$$\frac{d}{dt^*}(\rho^*(1-x^*)T^*) = -c^*\gamma T^* + P^*(\gamma-1)\frac{dx^*}{dt^*} \tag{11}$$

where γ is the ratio of specific heats (its value must be calculated from the steam tables).

Equations (8) - (11) have been solved numerically using the conditions of the $P_o/P_o max = 0.6$ test in Figure 5. In dimensionless terms the necessary initial conditions and system parameters for this test are

$x^*(0) = 0$ $\quad$ $k = 0.5$
$V^*(0) = 1$ $\quad$ $\gamma = 1.3$
$P^*(0) = 1$
$T^*(0) = 1$
$\rho^*(0) = 1$

The dimensional reference values for this test are

$P_o = 300$ kPa
$V_a \simeq 17$ m/s
$\ell_o \simeq 0.9$ m

It is important to note that c*, the dimensionless rate of mass transport from the steam to the liquid, is an input to the equations. Figure 10b shows predicted bubble collapse pressure histories for

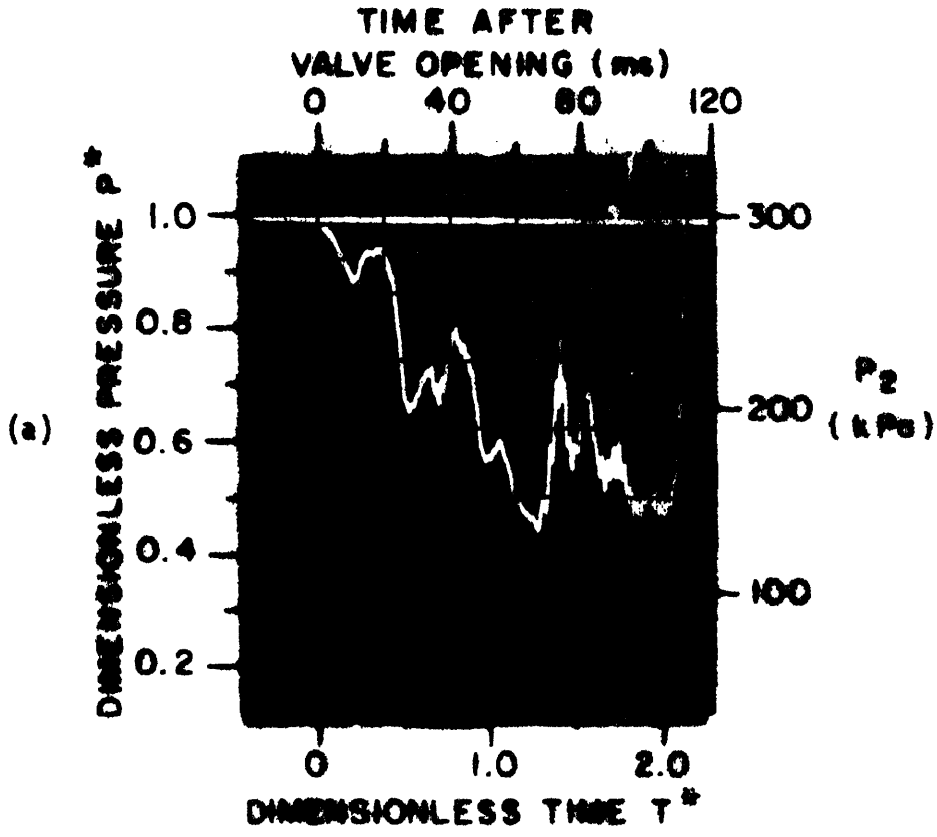

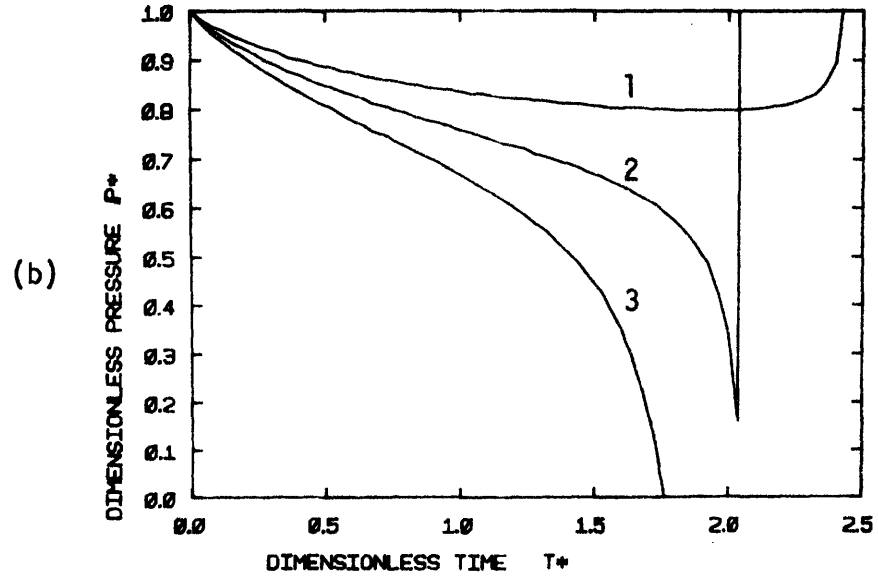

Figure 10. Dimensionless Bubble Collapse Pressure Histories
(a) Experimental trace for conditions in Figure 5 with $P_o/P_{omax} = 0.6$.
(b) Model predictions for same conditions, varying c*. Curve 1, c* = .404; Curve 2, c* = .485; Curve 3, c* = .566

three different values of c*: c* = .404, .485, and .566 . These values correspond to heat transfer rates ($-\dot{q} = \dot{m}_c h_{fg}/A$, where h_{fg} is the enthalpy of vaporization) of 25, 30 and 35 MW/m^2.

Comparing the predictions in Figure 10b with the experimental pressure trace in Figure 10a, it is clear that agreement is good when $-\dot{q}$ = 30 MW/m^2. This simulation produces fairly accurate pressure amplitudes over most of the collapse process and produces a collapse time almost identical to that observed experimentally.

Figure 11 shows corresponding calculated position, velocity and pressure histories for $-\dot{q}$ = 30 MW/m^2. The velocity at impact is V* = 0.68, or $V_I \simeq 12$ m/s. This predicted impact velocity can be compared with the experimentally measured initial impact pressure. The initial impact pressure (P_I) measured in the steel pipe is related to the impact velocity (V_I) in the lexan section by (Appendix II)

$$P_I = \rho_\ell V_I c_l c_s/(c_l+c_s) \qquad (12)$$

where c_l and c_s are the respective wave speeds in the lexan tube ($c_l \simeq$ 460 m/s) and the steel pipe ($c_s \simeq$ 1370 m/s). The amplitude of the impact pressure predicted in this way ($P_I \simeq$ 4100 kPa) compares remarkably well with the actual impact pressures for these conditions as recorded in Figure 5, $P_o/P_o max$ = 0.6.

Use of a single condensation rate in the numerical calculation yields good agreement with the experimental data for the low back pressure case discussed above. Figure 5 shows, however, that as the back pressure is increased, the collapse process is characterized by a high initial pressure drop rate and a subsequent region where the pressure

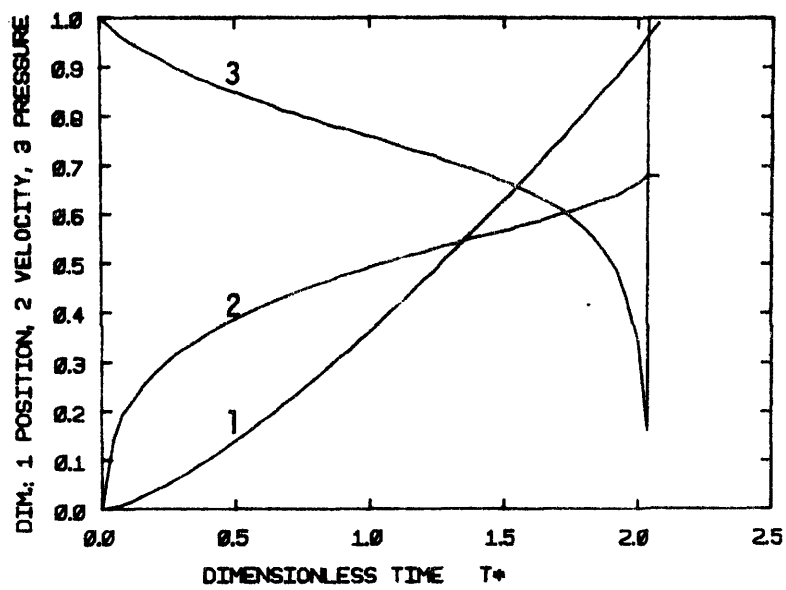

Figure 11. Dimensionless Bubble Pressure and Water Column Position and Velocity histories for $c^* = .485$ ($-\dot{q} = 30$ MW/m^2)

drop rate is much smaller, approaching zero for some of the cases (Figure 5). By analyzing these observed pressure drop rates (Figure 12), approximate net heat transfer rates from the steam to the water during different stages of the collapse process can be inferred. Modeling the steam as an ideal gas that is undergoing a heat loss per unit cross-sectional area $\dot{q}$ due to condensation at its interface with the liquid gives, very roughly (Appendix III),

$$\dot{q} = \frac{1}{\gamma-1}\left[(\ell_o - x)\frac{dP_s}{dt} - \gamma P_s \frac{dx}{dt}\right] . \qquad (13)$$

The heat transfer rate during the initial depressurization ($\dot{q}_o$) is determined when dP/dt is given by $(dP/dt)_o$ (Figure 12) and x = dx/dt = 0. The heat transfer rate during the subsequent phase ($\dot{q}_s$) is determined when P is $\overline{P}$ (Figure 12) and x and dx/dt are given by $\ell_o/2$ and ℓ_o/t_c, resectively. These different phases are not very pronounced in the low back pressure tests, but are evident in the higher back pressure tests (Figure 5). An average condensation rate ($\overline{\dot{q}}$) can be found when P, x, and dx/dt are again given by $\overline{P}$, $\ell_o/2$, and ℓ_o/t_c, respectively, and dP/dt is given by $\left(\frac{\overline{dP}}{dt}\right)$ (Figure 12). Substituting the appropriate values of P, dP/dt, and t_c which are read from the oscillogram in 10a into Equation (13) along with those of γ and ℓ_o gives $-\dot{q}_o \simeq 40$ MW/m^2, $-\dot{q}_s \simeq$ 7 MW/m^2, and $-\overline{\dot{q}} \simeq 8$ MW/m^2. These values are tabulated in Table 2 along with the value used in the numerical solution for the low back pressure simulation.

Equation (13) suggests that in the early phases of bubble collapse the condensation rate can be inferred from the initial slope of the pressure history. Experimentally, this slope is found to increase with

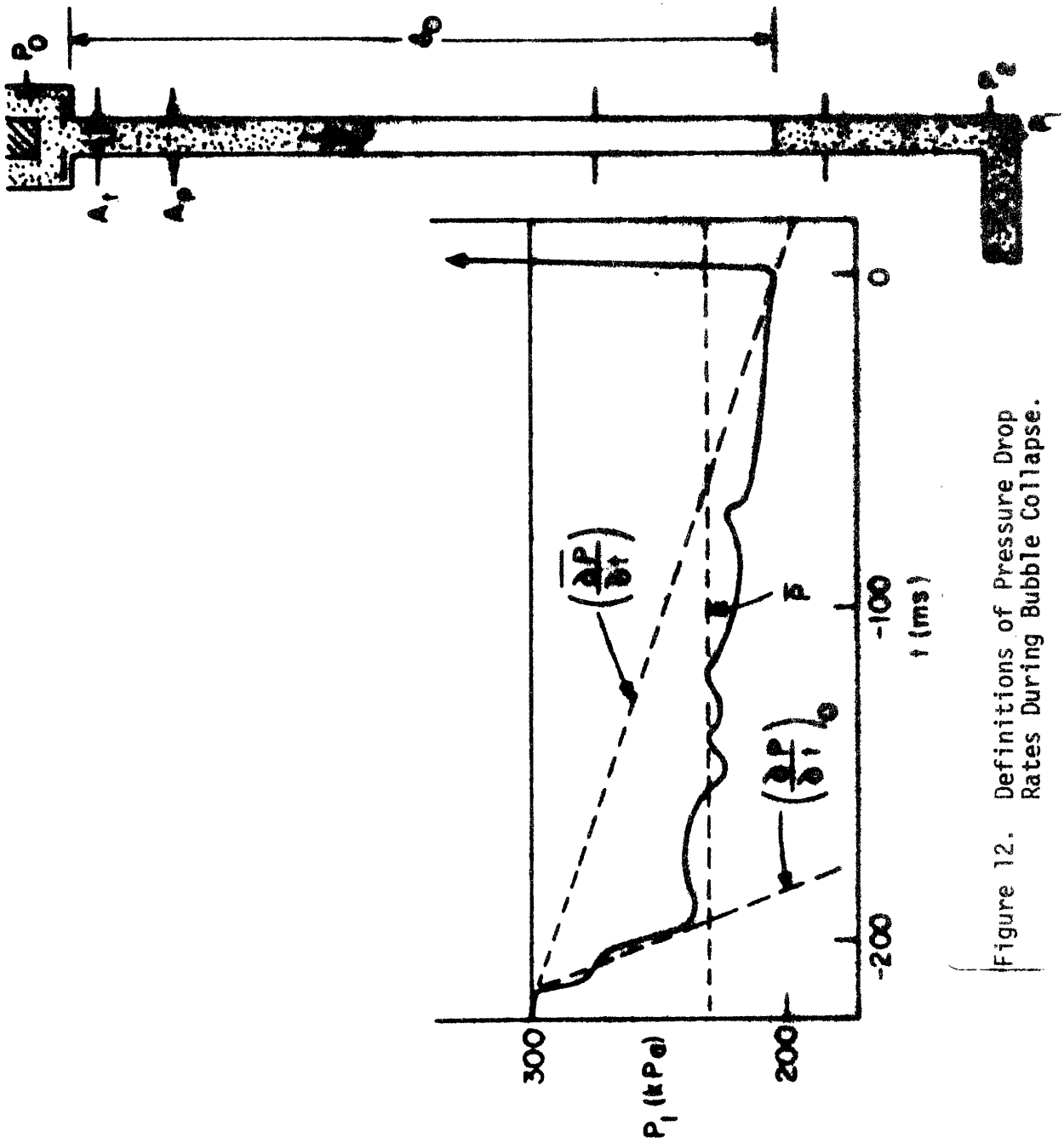

Figure 12. Definitions of Pressure Drop Rates During Bubble Collapse.

Table 2: Summary of condensation rate calculations for a low back pressure test ($P_o/P_o max$ = 0.6, Figure 5)

Condensation rate		(MW/m^2)
	$-\dot{q}_o$	40
Experimental	$-\dot{q}_s$	7
	$-\bar{\dot{q}}$	8
Numerical	$-\dot{q}$	30
Theoretical	$-\dot{q}_{vap}$	600
Estimates	$-\dot{q}_{turb}$	100

higher back pressures (Figure 5). For the highest back pressure experiment ($P_o/P_o max = 1.0$, Figure 5), the inferred initial heat transfer rate is $-\dot{q}_o \simeq 100$ MW/m^2, considerably higher than the initial heat transfer rate for the low back pressure test.

The initial and subsequent heat transfer rates could be controlled by two different rate limiting phenomena for heat transfer from steam to a liquid: transport of vapor to the subcooled liquid or turbulent convection in the liquid column.

If the transport of vapor is the rate limiting process:

$$-\dot{q}_{vap} = \frac{\sigma \rho_s h_{fg}}{4} \sqrt{\frac{8RT_1}{\pi}} \tag{14}$$

where σ is a constant with theoretical upper limit of 1.0 (Merte 1973). Substituting values corresponding to the test conditions in Figure 10b into Equation (14) gives $-\dot{q}_{vap} \simeq 600$ MW/m^2 (Appendix IV).

If turbulent convection in the liquid column provides the limiting heat transfer mechanism, a heat transfer of the following form is expected (Sonin and Kowalchuk 1978):

$$-\dot{q}_{turb} = \rho_\ell c \sqrt{\frac{\beta \bar{V} D}{t}} (T_1 - T_2) \tag{15}$$

Here c and $\bar{V}$ are the specific heat and mean velocity of the liquid, D is the pipe diameter, t is the elapsed time from the initiation of the heat transfer, and β is an empirical coefficient that relates the effective turbulent thermal diffusivity to the product $\bar{V}D$. For turbulent flows in pipes, β is expected to be of order 10^{-2} (Sonin and Kowalchuk 1978). Using V_I and t_c as characteristic column velocities and col-

lapse times, Equation (15) yields $-\dot{q}_{turb} \simeq 100$ MW/m^2 (Appendix IV).

These theoretically motivated estimates (Table 2) are an order of magnitude greater than the predictions from the numerical solution which gave the best agreement with the experimental results and from Equation (13). One factor that may account for much of this difference is boiling at the lower liquid interface during bubble collapse (Figure 4) which decreases the effective net mass transfer rates. The theoretical estimates do, however, provide consistant upper bounds at least for the conditions of these tests.

Independent experiments by Anderson (1980) support the condensation rates inferred from these experiments (summarized in Table 2). His apparatus is shown in Figure 13. Saturated steam is injected into a submerged vertical tube which induces "chugging" (a cyclic phenomenon whereby steam slowly fills the tube and at some point collapses rapidly). Normalized condensation rates for a pool temperature of 25°C and saturated steam at atmospheric pressure injected at a flux of 1 kg/m^{2}sec are shown in Figure 14. Measured condensation rates under these conditions were of order 20 - 40 MW/m^2, although some rates were found as high as 90 MW/m^2. These higher rates correspond roughly to the initial condensation rates predicted by Equation (13) for the case of highest back pressure ($-\dot{q}_o \simeq 100$ MW/m^2), while the majority of the rates (20 - 40 MW/m^2) correspond to the rates predicted by Equation (13) for the low back pressure test ($-\dot{q}_o \simeq 40$ MW/m^2) and by the numerical solution which gave the best agreement with the experimental results ($-\dot{q} \simeq 30$ MW/m^2).

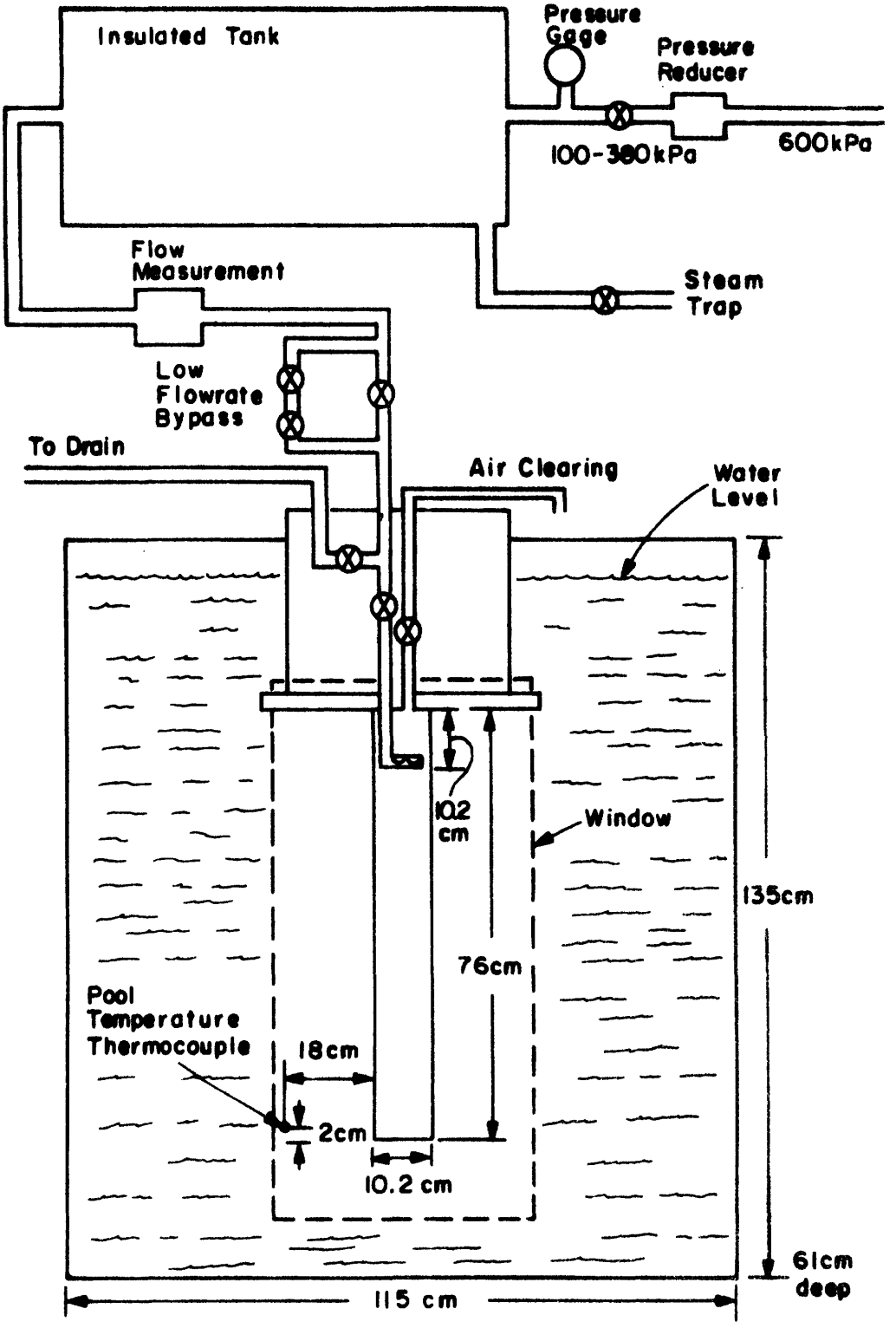

Figure 13. Schematic of "Chugging" Apparatus (Anderson 1980).

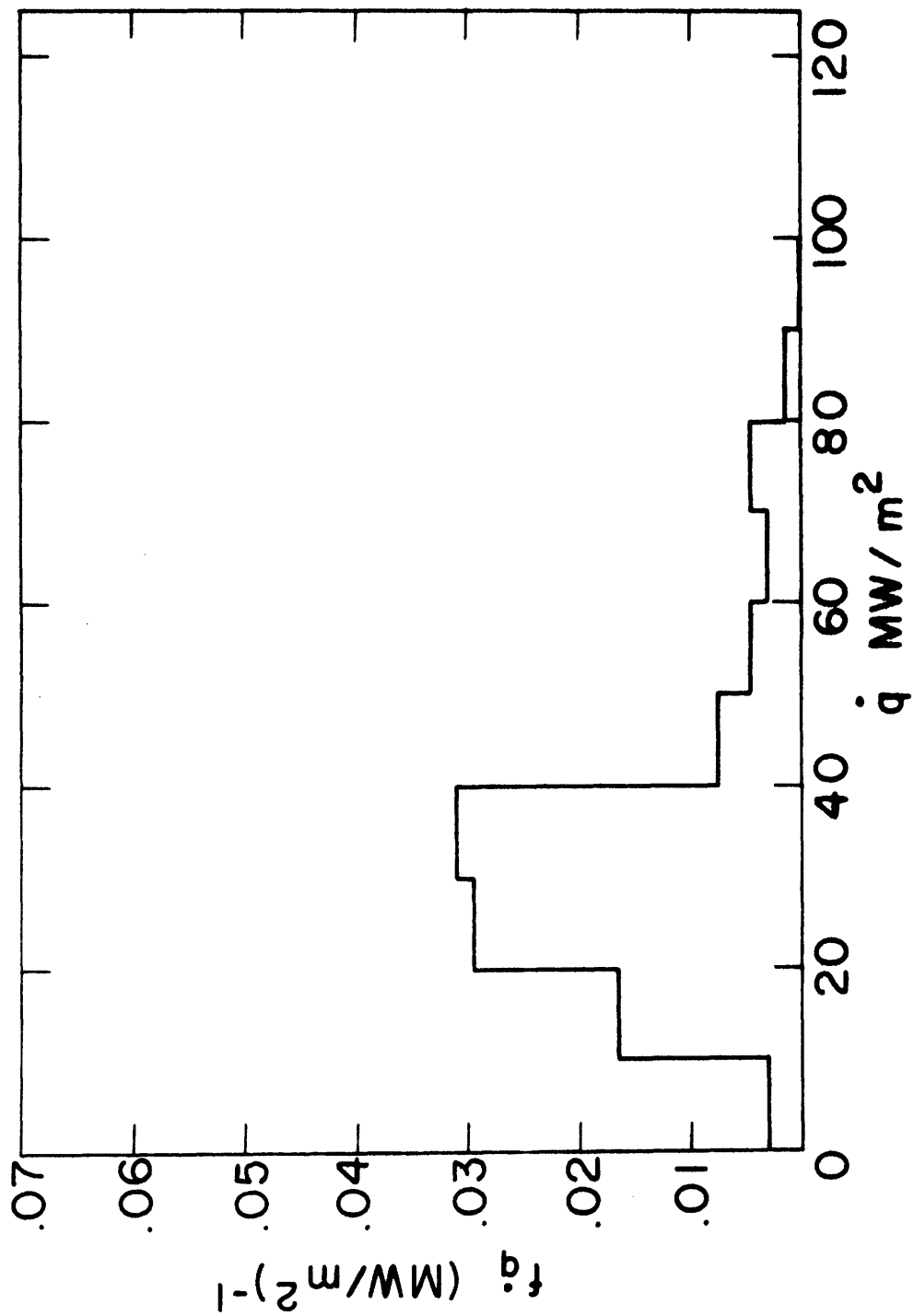

Figure 14. Probability Density function ($f_{\dot{q}}$) of heat transfer rates ($\dot{q}$) as measured by Anderson (1980) in "chugging" tests.

VII. Conclusions

Impact pressures and collapse times scale well with back pressure and flow resistance according to the proposed scaling parameters. Higher back pressures and lower flow resistances produce higher impact pressures and shorter collapse times.

The bubble collapse process is also very sensitive to the condensation rates from the steam to the subcooled liquid. Good agreement between prediction and experiment was obtained for one set of test conditions using a simple heat transfer rate as the sole empirical input to the analytical model. Other collapse conditions appear to exhibit heat transfer rates that decrease during the collapse history. The condensation rates that produce the "best fit" with the experimental data are consistantly below the condensation rates predicted by two theoretically predicted limits.

REFERENCES

Anderson, W. G., private communication, April, 1980.

Baumeister, T., and Marks, L. S., Standard Handbook for Mechanical Engineers, Seventh Edition, McGraw-Hill, New York.

Creare, Inc., "An Evaluation of PWR Steam Generator Water Hammer," NUREG-0291, NRC-1, May 1977.

Hurwitz, W., "Piping Network Response to Steam Generated Water Hammer," M.S. thesis, Department of Mechanical Engineering, M.I.T., May, 1980.

Merte, Jr., H., "Condensation Heat Transfer," in Advances in Heat Transfer (T. F. Irvine and J. P. Hartneft, eds.), Vol. 9, Academic Press, New York, 1973, pp. 181-272.

Sonin, A. A., and Kowalchuk, W., "A Model for Condensation Oscillations in a Vertical Pipe Discharging Steam into a Subcooled Water Pool," NUREG/CR-0221, June 1978.

Appendix 1: Derivation of Dimensionless Governing Equations

Unsteady Bernoulli:

$$P_o/\rho_\ell + gh = P_s/\rho_\ell + 1/2\ (1+k)\ V^2 + x\ dV/dt \tag{4}$$

$$1 + \rho_\ell gh/P_o = P_s/P_o + 1/2\ (1+k)(\rho_\ell/P_o)(dx/dt)^2 + (\rho_\ell/P_o)\ x\ d^2x/dt^2$$

For these tests $\rho_\ell gh/P_o \simeq 0.007$. Gravitational effects are small compared to back pressure and can be neglected.

$$1 = P^* + 1/2\ (1+k)\ V_a^{-2}\ (V_a dx^*/dt^*)^2 + V_a^{-2}\ x\ (V_a^2\ d^2x^*/dt^{*2})$$

$$1 = P^* + 1/2\ (1+k)(dx^*/dt^*)^2 + x\ d^2x^*/dt^{*2} \tag{8}$$

Steam bubble continuity:

$$-\dot{m}_c = d/dt\ (\rho_s A(\ell_o - x)) \tag{5}$$

$$-\dot{m}_c/\rho_s(0)AV_a = V_a^{-1}\ (V_a/\ell_o)\ d/dt^*\ \left[(\rho_s/\rho_s(0))(\ell_o - x)\right]$$

$$-c^* = d/dt^*\ (\rho^*(1-x^*)) \tag{9}$$

State equation:

$$P_s = \rho_s R T_1 \tag{6}$$

$$P_s/P_o = (\rho_s/\rho_s(0))(\rho_s(0)RT_1/P_o)$$

$$P^* = \rho^* T^* \tag{10}$$

Energy equation:

$$d/dt\ (\rho_s A(\ell_o - x)c_v T_1) = -\dot{m}_c c_p T_1 - P_s\ d/dt\ (A(\ell_o - x)) \tag{7}$$

$$\frac{R}{AV_a P_o}\frac{d}{dt}\left[\frac{\rho_s}{\rho_s(0)}A(\ell_o - x)c_v\rho_s(0)T_1\right] = \frac{R}{AV_a P_o}\left[-\dot{m}_c c_p T_1 - P_s\frac{d}{dt}(A(\rho_o - x))\right]$$

$$\frac{\ell_o}{V_a}\frac{d}{dt}(\rho^*(1-x^*)c_v T^*) = -\frac{\dot{m}_c}{\rho_s(0)AV_a}c_p\frac{\rho_s(0)RT_1}{P_o} + \frac{P_s}{P_o}\frac{R\ell_o}{V_a}\frac{dx^*}{dt^*}$$

$$d/dt^*\ (\rho^*(1-x^*)T^*) = -c^*\ \gamma T^* + P^*\ (\gamma - 1)\ dx^*/dt^* \tag{11}$$

Appendix II: Perturbation Analysis

The linearized perturbation equations at an interface separating regions with different wave speeds give the relationships between the velocities and pressures across the interface.

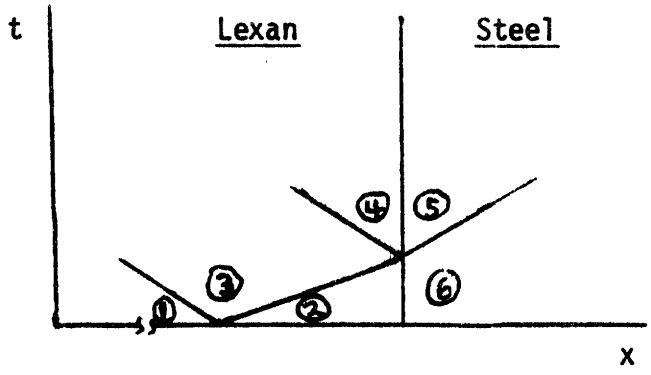

Wave speeds: $c_l \simeq 460$ m/s

$c_s \simeq 1370$ m/s

Linearized perturbation equations:

$$P_3 - P_1 = \rho c_l (V_1 - V_3) \quad \text{(a)}$$

$$P_3 - P_2 = \rho c_l (V_3 - V_2) \quad \text{(b)}$$

$$P_4 - P_3 = \rho c_l (V_3 - V_4) \quad \text{(c)}$$

$$P_5 - P_6 = \rho c_s (V_5 - V_6) \quad \text{(d)}$$

Boundary conditions: $V_2 = V_6$, $V_4 = V_5$

$P_2 = P_6$, $P_4 = P_5$

Initial conditions: $P_1 \simeq 0$, $P_2 = P_6 \simeq 0$ compared to P_3

$V_1 = V_I$, $V_2 = V_6 = 0$

Utilizing the initial conditions, Equations (a) and (b) become:

$$P_3 = \rho c_1 (V_1 - V_3) \quad (e)$$

$$P_3 = \rho c_1 V_3 \quad (f)$$

Combining Equations (e) and (f) yields:

$$\rho c_1 (V_1 - V_3) = \rho c_1 V_3$$

$$V_3 = V_1/2 \quad (g)$$

Utilizing the boundary conditions, Equation (c) becomes:

$$P_5 - P_3 = \rho c_1 (V_3 - V_5)$$

$$P_5 = P_3 + \rho c_1 (V_3 - V_5) \quad (h)$$

Utilizing the initial conditons, Equation (d) becomes:

$$P_5 = \rho c_s V_5$$

$$V_5 = P_5/\rho c_s \quad (i)$$

Combining Equations (h) and (i) yields:

$$P_5 = P_3 + \rho c_1 (V_3 - P_5/\rho c_s)$$

$$P_5(1 + c_1/c_s) = P_3 + \rho c_1 V_3$$

$$P_5 = (P_3 + \rho c_1 V_3)/(1 + c_1/c_s) \quad (j)$$

Combining Equations (f) and (j) yields:

$$P_5 = (\rho c_1 V_3 + \rho c_1 V_3)/(1 + c_1/c_s)$$

$$P_5 = 2\rho(c_1 c_s/c_1 + c_s) V_3 \quad (k)$$

Combining Equations (g) and (k) yields:

$$P_5 = 2\ \rho(c_1 c_s/c_1 + c_s)(V_1/2)$$

$$P_5 = \rho(c_1 c_s/c_1 + c_s) V_1$$

From the numerical simulation, $V_I \simeq 12$ m/s. Also, $P_5 = P_I$, so

$$P_I = \rho(c_1 c_s/c_1 + c_s) V_I \quad (12)$$

$$P_I = (1000\ \text{kg/m}^3)[(460 \cdot 1370)/(460+1370)\ \text{m/s}](12\ \text{m/s})$$

$$P_I \simeq 4100\ \text{kPa}$$

Appendix III: Condensation Rate Calculation

Energy equation for steam bubble:

$$d/dt\ [\rho_s A(\ell_o - x)c_v T_1] = -\dot{m}_c c_p T_1 - P_s\ d/dt\ [A(\ell_o - x)] \qquad (7)$$

Modeling the steam as an ideal gas gives $\rho_s T_1 = P_s/R$, and noting that $-\dot{m}_c c_p T_1$ can be represented as $\dot{q}A$, Equation (7) becomes

$$\frac{d}{dt}\left[P_s A(\ell_o - x)\ \frac{1}{\gamma - 1}\right] = \dot{q}A - P_s \frac{d}{dt}\left[A(\ell_o - x)\right]$$

Assuming constant γ gives;

$$\frac{A}{\gamma - 1}\left[(\ell_o - x)\ \frac{dP_s}{dt} - P_s \frac{dx}{dt}\right] = \dot{q}A + P_s A \frac{dx}{dt}$$

$$\dot{q} = \frac{1}{\gamma - 1}\ (\ell_o - x)\ \frac{dP_s}{dt} - \left[\frac{1}{\gamma - 1} + 1\right] P_s \frac{dx}{dt}$$

$$\dot{q} = \frac{1}{\gamma - 1}\left[(\ell_o - x)\frac{dP_s}{dt} - \gamma P_s \frac{dx}{dt}\right] \qquad (13)$$

Appendix IV: Evaluation of $\dot{q}_{vap}$ and $\dot{q}_{turb}$

$\underline{\dot{q}_{vap}}$:

$$-\dot{q}_{vap} = \frac{\sigma \rho_s h_{fg}}{4} \sqrt{\frac{8RT_1}{\pi}} \tag{14}$$

Modeling the steam as an ideal gas, $RT_1 = P_s/\rho_s$, gives:

$$-\dot{q}_{vap} = \frac{\sigma \rho_s h_{fg}}{4} \sqrt{\frac{8P_s}{\pi \rho_s}}$$

For saturated steam at $P_s = 300$ kPa, $\rho_s = 1.651$ kg/m^3

$h_{fg} = 2163.8$ kJ/kg

Using these values gives $-\dot{q}_{vap} \simeq 600$ MW/m^2 for $\sigma = 1$.

$\underline{\dot{q}_{turb}}$:

$$-\dot{q}_{turb} = \rho_\ell c \sqrt{\frac{\beta \bar{V} D}{t}} \, (T_1 - T_2) \tag{15}$$

Substituting V_I and t_c for $\bar{V}$ and t gives:

$$-\dot{q}_{turb} = \rho_\ell c \sqrt{\frac{\beta V_I D}{t_c}} \, (T_1 - T_2)$$

where $\rho_\ell \simeq 1000$ kg/m^3

$c \simeq 4200$ J/kg°C

$\beta \simeq 10^{-2}$

$D \simeq 0.04$ m

$T_1 - T_2 \simeq 110$°C

$V_I \simeq 12$ m/s

$t_c \simeq 0.1$ s

Using these values gives $-\dot{q}_{turb} \simeq 100$ MW/m^2.